A&A 474, 415–429 (2007)
DOI: 10.1051/0004-6361:20077497
© ESO 2007

Astronomy & Astrophysics

Magnetic fields and gas in the cluster-influenced spiral galaxy NGC 4254

I. Radio and X-rays observations⋆

K. T. Chyży[1], M. Ehle[2], and R. Beck[3]

[1] Astronomical Observatory, Jagiellonian University, ul. Orla 171, 30-244 Kraków, Poland
e-mail: chris@oa.uj.edu.pl
[2] XMM-Newton Science Operations Centre, ESA, PO Box 78, 28691 Villanueva de la Cañada, Madrid, Spain
[3] Max-Planck-Institut für Radioastronomie, Auf dem Hügel 69, 53121 Bonn, Germany

Received 16 March 2007 / Accepted 6 August 2007

ABSTRACT

Aims. Radio observations can show how cluster galaxies are affected by various environmental factors, that perturb their morphology, as well as modify properties of the interstellar medium (ISM), especially the characteristics of its magnetic field.
Methods. We made high-resolution and high-sensitivity radio-polarimetric VLA observations of NGC 4254 at three frequencies (8.46, 4.86, and 1.43 GHz). The interferometric data were extended with single-dish (100-m Effelsberg) observations. Next we performed sensitive XMM-Newton observations in X-rays and UV light to investigate the hot gas component and its possible interaction with the hot cluster medium. For a complete picture of the interplay between various gas phases, we also used optical, H I, and infrared (Spitzer) data.
Results. The distribution of total radio intensity at 8.46 GHz and 4.86 GHz reveals a global asymmetry with a more diffuse and almost two times larger extension to the north than to the south. The radio-polarized intensity is even more asymmetric, showing a strange bright ridge in the southern disk edge, displaced to the downstream side of the local density wave. Magnetic arms can also be seen in other disk portions, mostly (but not always) avoiding nearby optical spiral arms. Spatially-resolved emission of hot X-ray gas from the whole galactic disk, with its soft component closely tracing star-forming regions, is detected. Various gas components of a thermal origin show strong wavelet crosscorrelations ($r_w \geq 0.8$), but the polarized intensity anticorrelates ($r_w = -0.4$) with the thermal and X-ray emission. The slope of the local radio nonthermal-infrared relation is <1, thus smaller than for the radio thermal-infrared one (≥1). Using the radio thermal emission-based star-formation rate (SFR), we find higher extinction in more Hα luminous star-forming regions with a power-law slope of 0.83. The galaxy's estimated mean *SFR* of 0.026 $M_\odot$ yr^{-1} kpc^{-2} is three times larger than in other spirals with a similar Hubble type.
Conclusions. NGC 4254 seems to belong to the class of "young" Virgo cluster members, which recently experienced a gravitational encounter at the cluster's periphery, which in turn perturbed its spiral arms by tidal forces and triggered a burst of star formation that still maintains strong radio and infrared emissions. Tidal forces could also shear the magnetic field in the southern disk portion and lead to the observed polarized ridge, although magnetic field compression by weak ram pressure forces of the cluster gas cannot be excluded. The case of NGC 4254 shows that the polarized signal provides additional information on the MHD processes acting on magnetized plasma during the galaxy's evolution, which cannot be obtained from any other ISM component.

Key words. galaxies: general – galaxies: ISM – galaxies: magnetic fields – galaxies: interactions – radio continuum: galaxies – ISM: magnetic fields

1. Introduction

Galaxies in clusters are known to be affected by a number of environmental factors, which may change the galaxy's star-forming activity, leading to H I deficiency, spatial truncation of Hα emitting gas, morphological transformations, and strong dynamical galaxy evolution (Boselli & Gavazzi 2006). The ISM of disk galaxies in clusters can be altered by the cluster's ram-pressure stripping and/or by the galaxies' gravitational interactions redistributing the stellar and the gaseous disk content (Kenney et al. 2004; Vollmer et al. 2001). Investigating such galaxies at various wavelengths enables one to recognize particular physical processes at work within the perturbed ISM, and to provide a tentative scenario of the galaxy's interaction with the cluster medium (Machacek et al. 2004).

High-quality observations at radio frequencies are of special interest as they enable us to separate the thermal part of radio emission, thus providing a precise tracer of star-forming activity within galactic disks, unaffected by dust extinction. The polarized radio emission can reveal the regular magnetic field and its response to peculiar gas flows, giving independent insight into the disturbing agents in cluster spirals (Chyży et al. 2006).

The Virgo Cluster is the nearest moderately rich cluster with more than a hundred bright spirals and lenticulars. It is dynamically young with infalling galaxies and merging subgroups (Binggeli et al. 1993), while showing, specific to clusters, high-velocity gravitational encounters and galaxies in the process of morphological transformation. Galaxies of disturbed Hα disks (Koopman & Kenney 2004) or H I gas depletion

⋆ Figures 14 and 15 are only available in electronic form at http://www.aanda.org

Article published by EDP Sciences and available at http://www.aanda.org or http://dx.doi.org/10.1051/0004-6361:20077497

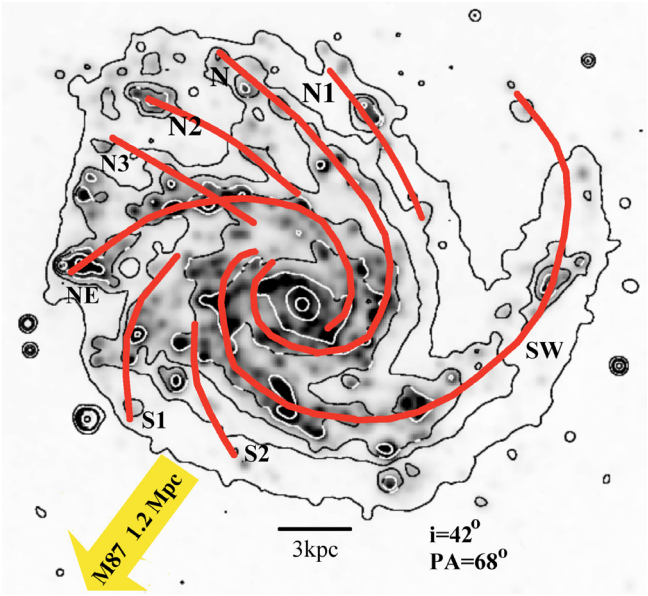

Fig. 1. Contour plot of the NIR IRAC 3.6 μm emission of the spiral (Sc) galaxy NGC 4254 overlaid on an Hα map at 4″ resolution (data from the Spitzer survey of SINGS galaxies, Kennicutt et al. 2003). The spiral arms (SW, N, NE) and arm-like features (N1, N2, N3, and S1, S2) are marked. The linear size scale, galaxy inclination, and position angle of the galactic major axis are also indicated.

(Cayatte et al. 1994) are ideal for studying the environmental processes affecting the galaxy evolution in detail.

The aim of this paper is to investigate the influence of the intracluster environment on the properties of radio emission and magnetic fields in the weakly disturbed Virgo Cluster spiral galaxy NGC 4254. The galaxy shows some external influence by its unusual optical spiral pattern (Fig. 1), dominated by a strange three-arm structure (SW, N, NE, Gonzáles & Graham 1996). The southern arm is particularly bright and thick with ongoing vigorous star formation. The northern and eastern parts of the galaxy show a number of weaker flocculent features, which makes the galaxy appear asymmetrical in optical images.

NGC 4254 is located far away from the Virgo centre – 3.7° (1.2 Mpc) in the NW direction from M 87 (Fig. 1). Its radial velocity of 2407 km s^{-1} (Phookun et al. 1993), when compared to the mean heliocentric velocity of the cluster of 1050 ± 35 km s^{-1} (Binggeli et al. 1993), gives an additional line-of-sight velocity component of about 1400 km s^{-1}. This value is approximately two times higher than the velocity dispersion of the cluster spirals, which can indicate that, if the galaxy has an orbital velocity typical of the Virgo Cluster galaxies, its actual velocity vector is almost tangential to the line of sight. As compared to the other cluster members, the galaxy shows a rather small H I deficiency (0.17, Cayatte et al. 1994), in agreement with the peripheral location of the galaxy within the cluster. However, the H I distribution of NGC 4254 is definitely asymmetric (Phookun et al. 1993) with a long extension to the north and a one-arm dominated spiral pattern. It has been proposed that the perturbed H I distribution could have been caused by tidal forces (Minchin et al. 2005) or tidal with ram pressure forces, due to the galaxy motion through the intracluster medium (ICM) (Vollmer et al. 2005).

Only low-resolution, single-dish radio observations of NGC 4254 at 10.45 GHz have been available up to now (Soida et al. 1996). They show some deviations in the total radio intensity from a symmetric disk, as well as regions of strong polarized emission. To investigate in detail the influence of the cluster medium on radio emission and magnetic field, we obtained sensitive three-frequency VLA radio polarimetric data. The interferometric data were merged with single-dish Effelsberg observations to recover the diffuse large-scale emission. We performed XMM-Newton observations in X-rays and UV light to study the hot medium. For a more complete picture we also re-processed the H I data from the VLA public archive and gathered Hα, optical (including HST), and infrared images from the Spitzer survey of SINGS galaxies (Kennicutt et al. 2003).

Spatial comparisons of radio total, thermal, and synchrotron components with the other ISM species were performed by the wavelet cross-correlation method (Sect. 4.3). We analysed the current state of star-forming processes by establishing the distribution of the extinction-free star-formation rate (SFR) *within* the galaxy, based on the radio thermal-emission data (Sect. 4.4). We also investigated the radio-infrared correlation diagram constructed for the regions within the galaxy and locate the galaxy on the global radio-infrared relation for a sample of non-interacting field spirals (Sect. 4.5). Finally, we estimated the relative importance of various competing internal and external forces at work in ISM by comparing the corresponding energy densities in the galactic disk and discuss possible interaction scenarios for the galaxy (Sect. 4.6).

In the sequel Paper II (Chyży 2007), we will investigate the Faraday rotation and various depolarization processes in NGC 4254 and analytically model the impact of ram-pressure and tidal forces on the galactic magnetic field.

2. Radio and X-ray observations and data reduction

To investigate the influence of the cluster medium on properties of radio emission and magnetic field in NGC 4254 we obtained radio and X-rays data. We give details of observations and data reduction process below.

2.1. VLA and Effelsberg data

High-resolution and high-sensitivity radio polarimetric observations of NGC 4254 were made at 8.46 GHz, 4.86 GHz, and 1.43 GHz using the VLA of NRAO[1]. The observations at 8.46 GHz and 4.86 GHz were performed in the D-array configuration and at 1.43 GHz with the C-array. All observations were carried out in the continuum mode with two independent channels of 50 MHz width (see Table 1 for details).

The intensity scale at all frequencies was calibrated by observing 3C 286. The position angle of linearly-polarized intensity was calibrated using the same source with an assumed position angle of 33°. At 4.86 GHz and 8.46 GHz, the calibrator 1236+077 was used to determine the telescope phases and instrumental polarization. In order to check these calibration procedures, 3C 138 was observed once each observing day.

The data reduction was performed using the AIPS data reduction package. The visibility data from each observational day were edited, calibrated, and self-calibrated in phase. The data from subsequent days were next combined, again self-calibrated in phase, and deconvolved to obtain maps in Stokes parameters I, Q, and U at all three frequencies. Adopting different weighting of UV data, with the robustness parameter (Briggs 1995) ranging from −1 to +1, maps with different resolutions and sensitivities

[1] National Radio Astronomy Observatory is a facility of National Science Foundation operated under cooperative agreement by Associated Universities, Inc.

Table 1. Parameters of VLA observations and exemplary resolution and rms noise in the final maps of I, Q, U Stokes parameters.

	Band 1	Band 2	Band 3
Frequency [GHz]	8.435 and 8.485	4835 and 4.885	1.385 and 1.465
Observing date	1997 Nov. 21; Dec. 12	1999 May 10	1998 Dec. 13
Configuration	D	D	C
Net observing time [h]	13.6	7.2	5.5
HPBW/σ_I, $\sigma_{Q,U}$ [μJy/b.a.]	10″/9, 7	15″/10, 9	17″/15, 8

were obtained. All maps were then corrected for primary beam attenuation. Typical rms noise in I, Q, and U maps, as well as beam sizes at all frequencies is given in Table 1.

In order to increase the sensitivity to extended structures, we performed additional observations with the 100-m Effelsberg radio telescope[2] at 4.85 GHz using the two-horn system. 16 coverages of 40′ × 30′ size were obtained for each horn during the observations in May and June of 1999. We also observed 3C 286 to establish the flux-density scale. The coverages from both the horns were edited by removing spikes of interferences and large-scale undulations in baseline levels. Next they were combined using the "software beam-switching" technique (Morsi & Reich 1986), followed by restoration of I, Q, and U maps. All the appropriate maps were then calibrated and combined using the spatial-frequency weighting method and digital filtering process to remove the spatial frequencies corresponding to structures smaller than the Effelsberg beam (153″ HPBW). The rms noise level in the final map of total intensity is 0.5 mJy/b.a. and 0.07 mJy/b.a in Q and U maps. In a similar way we also rereduced and calibrated the Effelsberg observations of NGC 4254 at 10.45 GHz of 65″ resolution obtained by Soida et al. (1996) to ensure that all the data we used were fully compatible.

In the UV plane we merged the I, Q, and U – VLA data at 8.46 GHz and 4.86 GHz with single-dish observations at 10.45 GHz and 4.85 GHz, respectively. The brightness values at 10.45 GHz were rescaled to 8.46 GHz assuming a spectral index of 0.8 ($\propto\nu^{-\alpha}$). The spectral index may vary locally, but the VLA data cover spatial frequencies well down to 1.1 kλ (which corresponds to a baseline of 40 m and angular resolution of 3′), hence the Effelsberg images add only the very diffuse signal on larger scales. Taking the inner one-third of the galaxy extent and changing the spectral index e.g. to 0.7 would result in the total signal increasing by 2%. For the polarized intensity, which is less extended than the total one, any errors of a similar kind are expected to be even less. As the Faraday rotation measures are small in this galaxy (up to about 100 rad m^{-2}, Paper II) the rescaling of the Effelsberg map may introduce a polarized angle offset up to 3°. None of those potential errors could change any conclusion of this paper.

We compared different methods of merging our interferometric and single-dish data using AIPS task IMERG and MIRIAD task IMMERGE, which differ in ways of weighting the data in the Fourier space. We chose the second method, which better filled the regions of negative VLA response around the high-gradient emission in the southern outer parts of the galactic disk and precisely recovered the total flux out of the single dish data. The merged I, Q, and U maps were then combined to get the distributions of total and linearly polarized intensities, as well as the position angle of magnetic vectors (not corrected for Faraday rotation $\boldsymbol{B}$-vectors, i.e. observed $\boldsymbol{E}$-vectors rotated by 90°).

The VLA H I data of NGC 4254 published by Phookun et al. (1993) with a velocity resolution of 10 km s^{-1} and spatial resolution of 35″ are not sufficient for a detailed comparison either with our radio data (with at least 15″ resolution) or with the X-ray and optical images. Therefore, we reduced the original VLA archived H I data from the VLA C and D arrays again. We used the standard approach to calibration, cleaning, and combining the data from both arrays, as well as to continuum subtraction procedures using AIPS. The final cleaned H I cube with uniform weighting had a resolution of 15″ and was used to derive the velocity-integrated H I intensity distribution, velocity field and velocity dispersion.

2.2. XMM-Newton data

2.2.1. X-ray data

On the 29 June 2003, we observed NGC 4254 with XMM-Newton[3] in the energy band of 0.2−12 keV and with about a 25′ × 25′ field of view (Observation Id: 0147610101). The EPIC MOS cameras (Turner et al. 2001) were used in "Full Frame" and the pn camera (Strüder et al. 2001) in "Extended Full Frame" mode with thin filters for the scheduled observing time of 52 ks. The Science Analysis System (SAS) version 6.0.0 was used to calibrate and analyse the data. As the observations were affected by high radiation, the standard procedures mentioned in the SAS User's Guide to define good time intervals were followed. Applying these selections to our data resulted in a clean observing time of 18 ks for MOS and 14.8 ks for pn. MOS and pn data were exposure-corrected, merged, and smoothed with a Gaussian filter to 10″ HPBW resolution.

A detailed analysis of the XMM-Newton data including a discussion of all X-ray emission components and their spectral properties is beyond the scope of this paper and will be presented in Ehle et al. (in prep.).

2.2.2. Optical Monitor data

During the X-ray observations, NGC 4254 was also observed with the onboard XMM-Newton Optical Monitor (OM, Mason et al. 2001) in UV filters UVW1 (2905 Å), UVM2 (2310 Å), and UVW2 (2070 Å) in "full frame low resolution" mode. The exposure times were 3 ks, 6 ks and 18 ks, respectively. We used the SAS package omichain (Mason et al. 2001) for photometric reduction and construction of a composite image in each of the UV filter bands.

The star formation traced by the ultraviolet emission of NGC 4254 observed by the OM through the *UVW1* and *UVW2* filters is shown as overlays in Fig. 4 (right panel) and Fig. 2 (top-right panel), respectively. They resemble the Hα image (compare Fig. 5) but involve stars with intermediate masses

[2] The 100-m telescope at Effelsberg is operated by the Max-Planck-Institut für Radioastronomie (MPIfR) on behalf of the Max-Planck-Gesellschaft.

[3] XMM-Newton is an ESA science mission with instruments and contributions directly funded by ESA Member States and NASA (Jansen et al. 2001).

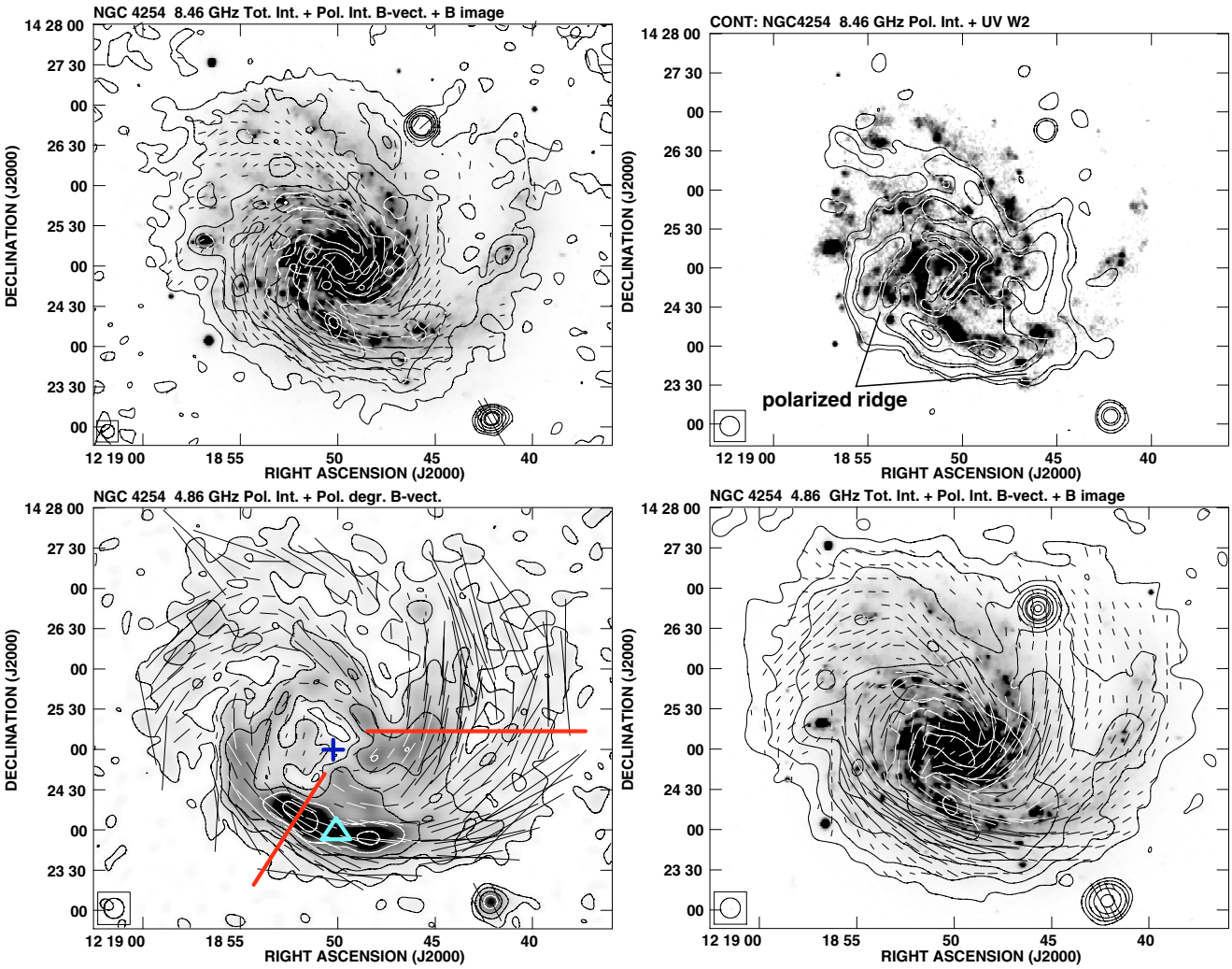

Fig. 2. *Top-left*: the contours of total radio intensity of NGC 4254 at 8.46 GHz with a resolution of 10″ and ***B***-vectors (not corrected for Faraday rotation) proportional to the polarized intensity overlaid on the optical blue image (from Knapen et al. 2003). The contours are at: 30, 80, 160, 320, 640, 1280 μJy/b.a. Vectors of length of 1″ correspond to a polarized intensity of 5 μJy/b.a. *Top-right*: the contours of polarized intensity at 8.46 GHz with a resolution of 15″ overlaid on the UVW2 image from our XMM satellite observations, denoting the ensembles of young stars. *Bottom-left*: the contours of total intensity at 4.86 GHz with a resolution of 15″ with ***B***-vectors proportional to the polarized emission overlaid on the optical *B*-image. The contours are at: 30, 80, 160, 320, 640, 1280 μJy/b.a. Vectors of length of 1″ correspond to a polarized intensity of 8.3 μJy/b.a. *Bottom-right*: the contours and greyscale of polarized intensity at 4.86 GHz with a resolution of 15″ with ***B***-vectors of percentage of polarization. The contours are at 30, 80, 160, 250 μJy/b.a. Vectors with a length of 1″ correspond to a polarization degree of 1%. The galaxy's centre is marked by a cross, while a triangle marks the region selected for energy density calculation (see Sect. 4.6.1). Two lines mark positions of performed slices (Sect. 4.3).

and with ages of about 100 Myr, the distribution of which is less clumped and which follows the outline of spiral arms even better.

3. Results

The following Sects. 3.1–3.3 present briefly the obtained maps of NGC 4254 in radio-total, polarized, and X-ray emission, and their correspondence to optical images.

3.1. Total radio intensity

Our combined VLA and Effelsberg map of total radio intensity of NGC 4254 at 8.46 GHz (Fig. 2, top left) shows a steep gradient of emission in the southern disk, where the long SW spiral arm is located (cf. Fig. 1). In the northern part of the disk, the radio emission is much more diffuse and extends 1.5 times further from the centre than in the southern one. The same kind of N–S asymmetry is revealed by the optical *B* image (Fig. 2, top left in greyscale). The global N–S asymmetry is further confirmed by a more sensitive radio map at 4.86 GHz (Fig. 2, bottom left). The asymmetric radio pattern is more diffuse in this case and extends roughly 20′ (1.6 kpc) further out than at 8.46 GHz.

Beyond the two brightest peaks in the radio images, which are background sources (see Table 2 for details), the galaxy's

Table 2. Total radio fluxes of NGC 4254 including the background sources (in mJy) and fluxes of the background sources alone at the three observed frequencies.

RA_{J2000}	Dec_{J2000}	8.46 GHz	4.86 GHz	1.43 GHz
Total flux		102 ± 5	162 ± 6	512 ± 19
12 18 55.06	14 28 52.0	n/a	1.1 ± 0.1	5.7 ± 0.1
12 18 45.70	14 26 44.6	4.0 ± 0.1	7.1 ± 0.1	22.4 ± 0.1
12 18 42.15	14 23 07.0	1.8 ± 0.1	2.1 ± 0.1	4.0 ± 0.1

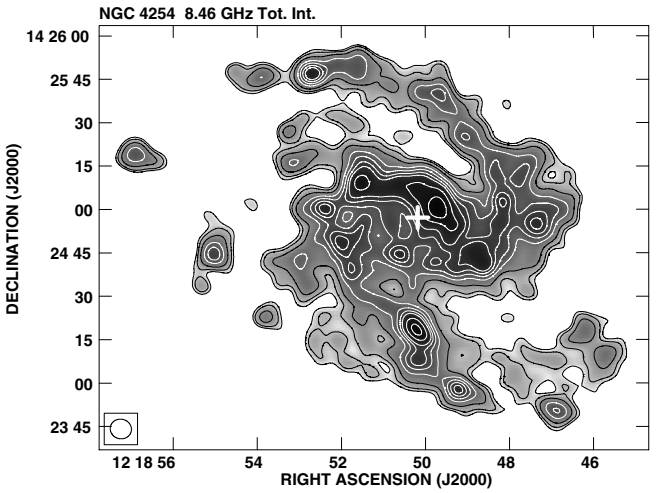

Fig. 3. The brightest structures in total radio intensity (greyscale and contours) of NGC 4254 at 8.46 GHz observed at the highest resolution of 7.″5. The contours are at: 120, 140, 180, 240, 300, 350, 400, 500, 600 μJy/b.a. The cross denotes the position of the optical centre of the galaxy.

centre alone is the strongest source on the radio maps. Contrary to the optical emission, which here shows numerous concentrations of star formation not forming any particular pattern, the radio emission is elongated and hosts a bar-like feature, from which two arms (SW and NE) emerge. This is most visible in our Fig. 3 of the central part of the disk with the highest resolution of 7.″5 (600 pc). The two radio arms form a clear and symmetric spiral pattern. They extend from the bar ends to the north and south and then wind tightly around the disk. Similar features can be seen in the integrated CO emission (Sofue et al. 2003), but not in the other ISM species.

Our 1.43 GHz total intensity map with 17″ HPBW resolution (Fig. 4) reveals a very extensive diffuse radio envelope of NGC 4254. The envelope is particularly stretched towards N, where the radio emission extends about 1′ (more than 4 kpc) further away than the optical emission in the disk. However, the radio envelope is traced surprisingly well by the H I emission (Fig. 4): not only the northern part but also two odd radio extensions to the NE (RA = $12^{\rm h}19^{\rm m}2^{\rm s}$, Dec = 14°27′50″) and to the SW (RA = $12^{\rm h}18^{\rm m}37^{\rm s}$, Dec = 14°24′0″) have H I counterparts. In the north, the H I gas extends further than the radio emission. Also, two H I blobs in the south (around RA = $12^{\rm h}18^{\rm m}57.5^{\rm s}$, Dec = 14°22′40″) have no radio counterparts. Both structures have H I radial velocities that differ by about 100 km s^{-1} from the adjacent gas in the disk (see Fig. 13). They could be related to some external perturbing agent, as was suggested by Phookun et al. (1993).

We integrated the radio total emission over the galaxy. Due to different sizes of the VLA antenna primary beam for different frequencies, we applied the integration area extending up to about 3.′5 in radius at 8.46 GHz, and up to 5′ at both 4.86 GHz and 1.43 GHz. The total radio fluxes at 4.86 GHz and 8.46 GHz are 162 ± 6 mJy and 102 ± 5 mJy, respectively. They are in a good agreement with the earlier works (e.g. Soida et al. 1996). The total integrated flux at 1.43 GHz is 512 ± 10 mJy. This value is higher than measured from the NVSS survey (418 mJy), due to the 10× better sensitivity of our present map. It is lower than the single-dish measurements (see Soida et al. 1996) most likely because of contamination from background sources in the previous low-resolution data. All background sources that can affect the integrated fluxes of NGC 4254 are presented in Table 2. The emission from background sources is subtracted in all subsequent analyses.

3.2. Polarized emission

The most characteristic feature of polarized radio emission at the high frequency of 8.46 GHz is a strong ridge with a double peak in the southern part of the galaxy (Fig. 2, top right). It shows a steep decrease in emission outwards from the disk. The ridge is clearly displaced by about 15″ (1.2 kpc) from the SW spiral arm and is located *outside* of it, on the downstream side of the density wave. The ridge has no counterpart in the total radio emission.

At the base of the N arm (around RA = $12^{\rm h}18^{\rm m}45^{\rm s}$, Dec = 14°25′0″, Fig. 2, top right), the highest polarization is found again outside the optical arm, like in the southern polarized ridge, on the downstream side of the density wave. In contrast, in the northern part of the same N optical arm (around RA = $12^{\rm h}18^{\rm m}49^{\rm s}$, Dec = 14°26′0″), the polarized emission is shifted *inwards* (to the east) from the spiral arm, thus to the upstream side of the density wave. Closer to the galaxy's centre, another strong elongated polarized feature is interlaced with the NE and SW spiral arms (around RA = $12^{\rm h}18^{\rm m}51^{\rm s}$, Dec = 14°25′45″).

At 4.86 GHz with higher sensitivity to extended structures, the polarized intensity covers almost the full optical extent of the galaxy (Fig. 2, bottom right). Opposite the southern polarized ridge, the northern galaxy portion is filled with much more diffuse emission without any strong polarized maxima. This global N–S asymmetry in intensity is about 6, which is larger than either in total radio emission (about 4) or in optical, Hα, and H I ones. This raises the question of whether the strong southern polarized ridge can result from the same perturbing agent as what causes the N–S asymmetry in other ISM components (see Sect. 4.6.3).

The $\boldsymbol{B}$-vectors of the ordered magnetic field[4] in NGC 4254 form quite a smooth spiral-like pattern coherently filling the very broad (optically very faint) interarm region between the SW and N spiral arms (Fig. 2, bottom left). As the Faraday rotation measure in NGC 4254 only occasionally exceeds 100 rad m^{-2} (Paper II), the observed directions of the magnetic field at 8.46 GHz and 4.86 GHz are close to the internal ones (the differences are up to 7° and 23°, respectively. The pitch angle of the observed magnetic field changes considerably throughout the galaxy from zero in the southern polarized ridge to about 40° in the northern part. However, the orientation of magnetic field is always close (within 20°) to the direction of the nearby optical spiral arm, indicating that it is connected to the direction of the density wave.

The galaxy's integrated polarized flux at 4.86 GHz is 21 ± 2 mJy, which gives the mean polarization degree p of 13.5 ± 0.5%. The southern ridge of NGC 4254 has a polarized flux of 3.1 ± 0.3 mJy, constituting about 15% of the galaxy's total polarized emission. The mean degree of polarization in the ridge is about 23.8 ± 0.5%, almost two times larger than the average over the whole galaxy. Without the ridge, the mean polarized fraction (in the rest of the galaxy) is 12.5%, hence the ridge enhances the galaxy mean polarized fraction by only one percent. The highest degree of polarization (up to some 40%) is found locally in the

[4] The ordered (regular) magnetic field observed in the polarized radio emission can consist of a unidirectional (coherent) field and a non-unidirectional anisotropic one. Faraday rotation is only sensitive to the coherent field component.

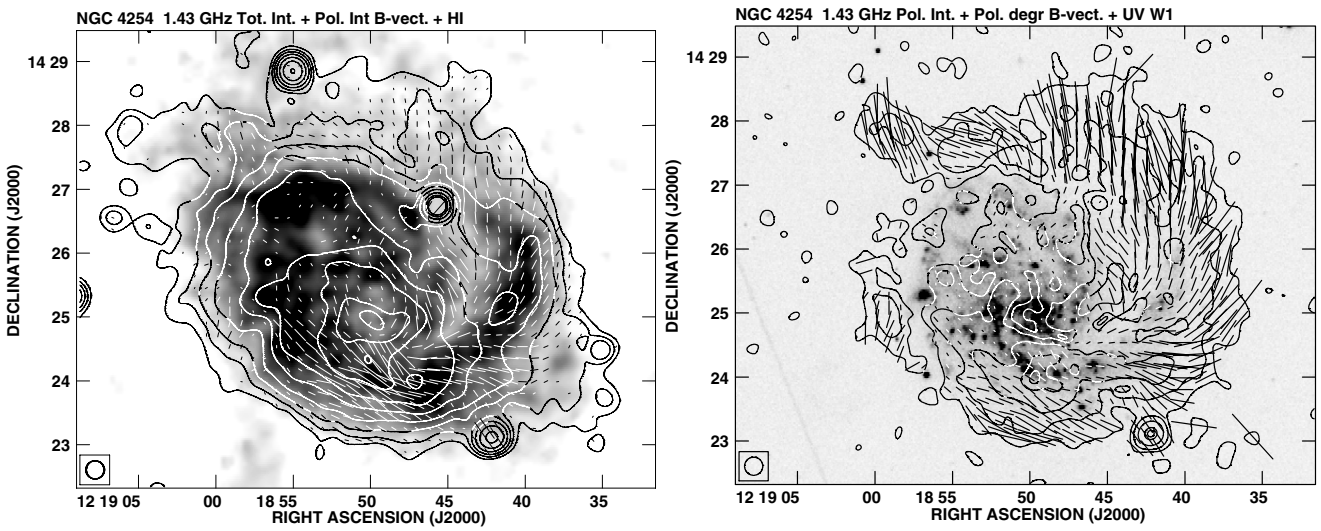

Fig. 4. *Left*: the total intensity map of NGC 4254 at 1.43 GHz in contours with ***B***-vectors (not corrected for Faraday rotation) overlaid on the H I line emission. The contours are 0.06, 0.16, 0.32, 0.64, 1.3, 2.6, 5.1, 8.0, 10.2 mJy/b.a. A vector of length of 1″ corresponds to polarized intensity of 12.5 μJy/b.a. *Right*: the polarized intensity contour map overlaid on the *UVW1* filter map from our XMM satellite observations with ***B***-vectors of polarization percentage. The contours are 25, 70, 190, 450, 550 μJy/b.a. A vector of length of 1″ corresponds to a polarization degree of 1%. The beam size is 17″ × 17″.

southern ridge and in the western interarm region (between the SW and N arms).

Our low-frequency 1.43 GHz data allow for a study of Faraday effects. At this frequency the Faraday rotation measure of 100 rad m^{-1} corresponds to the rotation of the magnetic field vectors by 253°. Indeed, except for the outer parts of the SW arm, the orientations of the magnetic field seen in Fig. 4 are unrelated to those observed at higher frequencies (Fig. 2, left). In contrast to the higher frequency maps, the 1.43 GHz polarized intensity map (Fig. 4, right) shows the strongly depolarized galaxy's centre ($p < 1\%$) and the NE portion of the disk ($p < 3\%$), where patchy spiral arms are visible in the optical image. The western part is less depolarized, especially in the vast western interarm region ($p \approx 13\%$) and outside of star-forming regions along the SW optical arm ($p \approx 10\%$). This gives a strongly asymmetric distribution of 1.43 GHz polarized emission with respect both to the galactic major axis and to the location of the optically bright SW spiral arm.

The 1.43 GHz data show another interesting feature: the reported extended envelope in the total radio intensity (Sect. 3.1) turns out to be polarized, forming an unclosed, ring-like structure. The high polarization degree of $p \approx 30{-}40\%$ indicates the presence of an ordered magnetic field extending further than the galactic gas traced by optical images. Similar polarized envelopes at 21 cm have been observed so far in M 83 (Neininger et al. 1993) and NGC 6946 (Beck 2007). The polarized envelope of NGC 4254 is the first one observed in a cluster spiral.

3.3. X-ray emission observed with XMM-Newton

Our XMM-Newton data show the most extended emission of NGC 4254 in soft energy bands (200−900 eV, Fig. 5). The X-rays reveals neither a feature outside the optical disk nor any association with the southern strong polarized ridge.

The X-ray emission is asymmetric: weak and diffuse in the north and stronger with a steeper gradient in the south. This pattern is similar to those seen in optical and Hα (Fig. 5) images and in total radio images (Sect. 3.1). Almost all X-ray features are associated with H II regions, and they are particularly strong in the central part of the disk and in the regions located in the NW and NE spiral arms within 1′ of the core. The central X-ray peak also corresponds well (in all energy bands) to the maxima in the optical and radio emission. (The strongest peak at RA = $12^{\rm h}18^{\rm m}56^{\rm s}$, Dec = 14°24′23″ has no counterpart in other wavebands and is probably due to an unrelated source.) The globally asymmetrical X-ray morphology and its correspondence with Hα distribution implies that the hot gas is closely connected to the star-forming activity. Both disturbed morphologies resemble the observed total radio intensity at 8.46 and 4.85 GHz (Sect. 3.1) and are likely to be caused by the same perturbing agent.

We do not find any X-ray background emission further out of the galactic disk out to a 10′ radius. This suggests that either NGC 4254 is situated outside the well-known hot envelope of the Virgo Cluster (Böhringer et al. 1994) or that the intergalactic medium is so tenuous that it cannot be directly detected even in our sensitive observations.

4. Discussion

Among all spiral non-barred galaxies mentioned in the recent reviews of galactic magnetism (Beck 2005; Vallée 2004; Widrow 2002), only about 10 have 1 kpc-scale radio polarimetric observations with enough sensitivity to cover almost the whole stellar disk. Out of those, only four (M 31, M 51, M 83, NGC 6946) have such high quality observations at three frequencies, like NGC 4254. None of them is a cluster member. In comparing the radio properties of NGC 4254 to other galaxies, we found that the phenomenon of polarized ridges shifted from optical spiral arms is very peculiar. To some extent the ridges resemble the observed magnetic arms in the non-interacting, non-cluster spirals: IC 342 (Krause et al. 1989; Krause 1993); and NGC 6946 (Beck & Hoernes 1996). The high degree of polarization in the southern ridge in NGC 4254 (up to $p = 40\%$ with a mean of 24%, Sect. 3.2) is also similar to the bright magnetic arms in NGC 6946 (40% and 28%, respectively, Beck & Hoernes 1996; Beck 2007). However, the southern polarized ridge in NGC 4254 is a very special feature. In typical grand-design spirals like NGC 6946 and also in some portions of NGC 4254, ordered

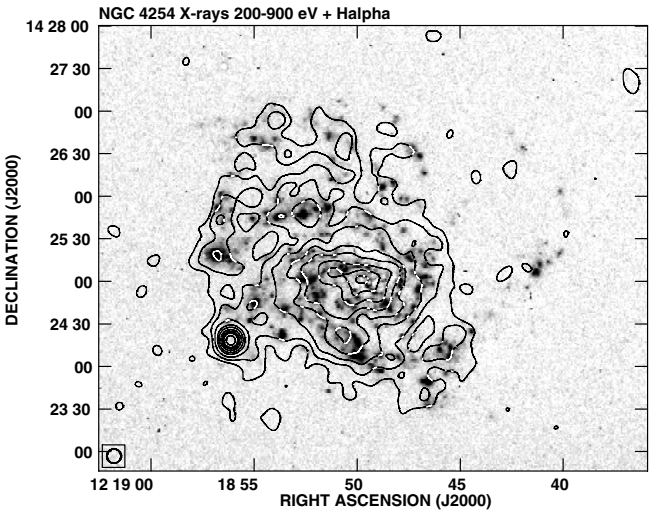

Fig. 5. X-ray XMM-Newton emission of NGC 4254 as seen by the combined EPIC cameras smoothed to a resolution of 10″. Contours of the soft (200−900 eV) emission are at (2.5, 4, 5.7, 8, 11.3, 16, 22.6, 32, 45.3, 64) × rms noise above the background and overlaid on the Hα image of NGC 4254 (from Knapen et al. 2004).

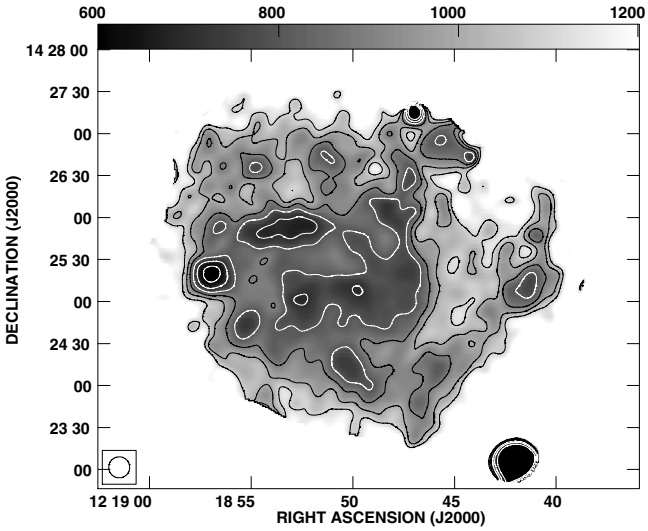

Fig. 6. Radio spectral index distribution between 4.86 and 1.43 GHz in NGC 4254 (contours and greyscale). Both maps of total intensity were convolved to a common beam of 15″. The contours are: 0.6, 0.7, 0.8, 0.9, 1.0, 1.1.

fields are strongest at the locations of prominent dust lanes on the inner edge of gaseous spiral arms (Beck 2005). But the strong southern ridge in NGC 4254 is located downstream of the density wave at the edge of the galactic disk (Fig. 2, top right), which can suggest some unknown, possibly external, process.

The southern ridge also drives a strong global N–S asymmetry in the polarized intensity. Such asymmetric polarization patterns have only been observed to date for some interacting galaxies such as NGC 3627 (Soida et al. 2001) or NGC 2276 (Hummel & Beck 1995). This implies some external interaction also in the case of NGC 4254. However in those galaxies the polarized signal is not shifted out of the bright optical disk.

In the most western portion of the disk, the polarized emission in NGC 4254 follows the optical spiral arm (see also Sect. 4.3). This resembles outer southern and southwestern spiral arms in M 51 (Patrikeev et al. 2006). Ordered fields coinciding with the outer optical arms were also reported for M 83 and NGC 2997 (Beck 2005). In short, the polarized properties of NGC 4254 are inhomogeneous and, besides the southern ridge, they show a mixture of structures observed in other galaxies.

Concerning the X-ray emission, we notice that the only other spiral-like galaxy in the Virgo cluster for which high-sensitivity X-ray data have been published is NGC 4438 (Machacek et al. 2004). This edge-on galaxy has a highly disturbed morphology in the stellar content, which is followed by Hα and X-ray emissions displaced up to 10 kpc from the disk's plane. The galaxy probably suffered from a strong off-centre collision with the nearby elliptical galaxy NGC 4435 about 100 Myr ago (Machacek et al. 2004). The X-ray emission in NGC 4254 also shows a close connection with the perturbed stellar disk and Hα gas, but the galaxy is not "damaged" like NGC 4438, which may suggest a much weaker interaction during a possible encounter (see Sect. 4.6.2).

Another process that could perturb NGC 4254 and its X-ray emission is ram pressure due to the motion of the galaxy through the hot ICM. An example of such a process at work can be seen in the case of NGC 2276, a member of the NGC 2300 group of galaxies. The Chandra X-ray observations reveal a bow shock feature along the western galactic disk with enhanced density and hot gas temperature (Rasmussen et al. 2006). This is also the location of shocked and compressed magnetized plasma, as the radio total and polarized emissions peak here (Hummel & Beck 1995). Furthermore, a tail of diffuse hot gas extends out of the galaxy on the opposite disk side. None of the X-ray features connected with the ram pressure forces in NGC 2276 (the leading bow shock and the hot tail) are present in the X-ray image of NGC 4254 (Fig. 5), which scores a point against strong ram pressure effects in this case.

Therefore, it is not easy to construct a single interaction scenario for NGC 4254. Some of its distinctive observed properties are either unknown among galaxies (the southern polarized ridge) or can vaguely indicate weak environmental effects of some kind (the X-ray emission). A more detailed analysis of this problem is presented below. We start with the discussion of the radio spectral index and go on the separation of thermal and non-thermal radio emission.

4.1. Spectral index distribution

The spectral index distribution in NGC 4254 (Fig. 6) has been determined for each map pixel according to a power law $S_\nu \propto \nu^{-\alpha}$ using the values of total intensity at 1.43 GHz and 4.86 GHz. At least half of the galactic regions have a steep radio spectrum with $\alpha \simeq 0.8$, which is also the mean galactic spectral index, typical of late-type spirals (e.g. Niklas et al. 1997). The spectrum flattens in the regions of spiral arms. Within the heavy concentrations of star formation visible in Hα emission, it reaches a slope of about 0.7, while it is just 0.64 in the nuclear region. The flattest spectrum of 0.55 is observed at the position of the strongest H II region at the tip of the NE arm (RA = $12^{\rm h}18^{\rm m}57^{\rm s}$, Dec = 14°25′19″). Its radio and X-ray emission is present but not too strong, which may indicate some very recent star-forming activity. Outside of spiral arms, the spectrum steepens, achieving the slope of about 1.2 on the disk's outskirts. In the characteristic large interarm space between the SW and N arms, the spectral index varies from about 1.0 to 1.1.

There is no global N–S asymmetry in the spectral index distribution like what is observed in total radio intensity. There is no evidence of cosmic ray (CR) acceleration or enhanced ageing

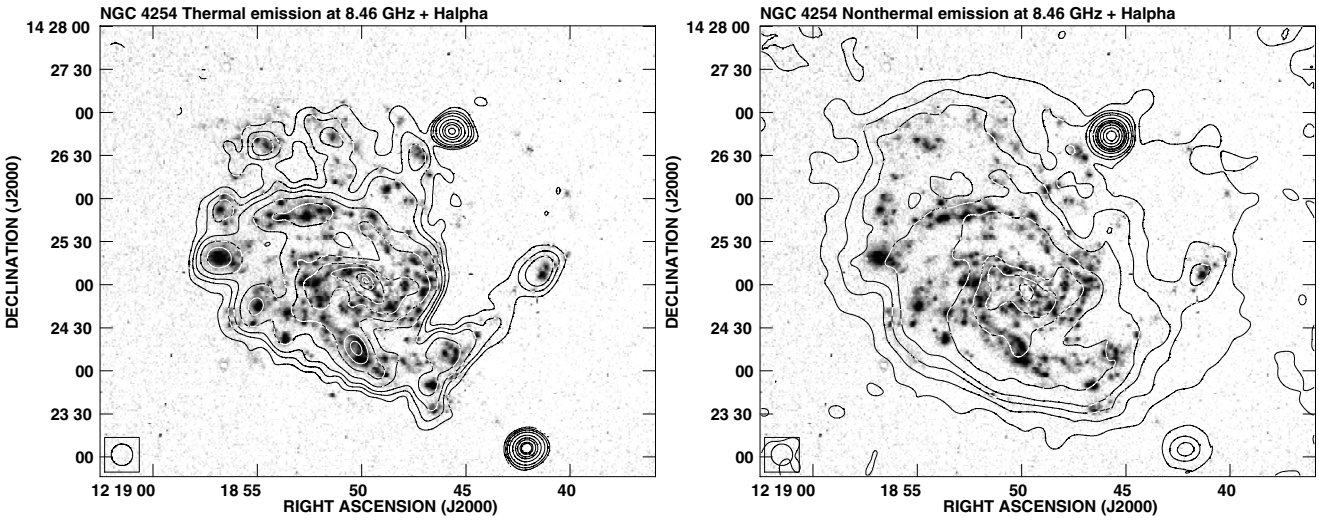

Fig. 7. Thermal (*left panel*) and nonthermal (*right panel*) radio intensity maps of NGC 4254 at 8.46 GHz overlaid on the Hα image. Contours are: *left panel*: 0.06, 0.16, 0.32, 1.2, 2.5 mJy/b.a.; *right panel*: 25, 70, 190, 450, 559 μJy/b.a. The beam size is $15'' \times 15''$.

of CRs in the southern polarized ridge, which would indicate a shock or strongly compressed magnetic field. Te spectral index of about 1.0 in this area is similar to that of typical interarm regions in the NE disk.

4.2. Thermal and nonthermal components

The distributions of synchrotron and thermal free-free radiation in NGC 4254 can be separated by least-square fits of thermal fraction on each of the map points of observed radio emission simultaneously at three frequencies. We assume that the nonthermal spectral index $\alpha_{\rm nth}$ is constant within the frequency range 1.43−8.46 GHz and throughout the galaxy (see e.g. Ehle & Beck 1993). The synchrotron spectrum is flatter in the spiral arms, which leads to overestimating the thermal intensity and underestimate the nonthermal one (Tabatabaei et al. 2007b). We performed the fitting procedure for various values of $\alpha_{\rm nth}$ from 0.95 to 1.1 and compared the derived distribution of radio thermal emission with the Hα map. The best correspondence in the interarm regions, where possible Hα dust attenuation is minimized, was achieved for $\alpha_{\rm nth} \approx 1.0 \pm 0.05$. We checked this value by two other methods. In the first approach we took the integrated fluxes at three frequencies and separated the global thermal and nonthermal components in a similar way to Niklas et al. (1997). This yields $\alpha_{\rm nth} = 1.0$. Next, we estimated $\alpha_{\rm nth}$ using our spectral index map (Fig. 6) taking the mean value in the large interarm region between SW and N arms as free from thermal emission. This gave $\alpha_{\rm nth} = 1.05$. Since all methods give consistent results, we finally use $\alpha_{\rm nth} = 1.0$.

A close similarity of the obtained radio thermal emission and Hα emitting gas (Fig. 7) confirms that the applied procedure cannot be significantly influenced by systematic effects. The thermal fraction at 8.46 GHz is typically up to about 25% in the interarm space and 35−55% within the spiral arms. The mean thermal fraction over the whole galaxy of 20% at 8.46 GHz is lower than the mean fraction of 30 ± 4% calculated for a large sample of disk galaxies by Niklas et al. (1997). However, systematically lower thermal fractions were found by Niklas (1995) in galaxies with higher star-formation rates, which is the case for NGC 4254 (see Sect. 4.4).

The distribution of nonthermal emission is remarkably smooth (Fig. 7), partly due to the CR diffusion process. However, it reaches up to different radii in different galaxy regions: about 2−2.5 kpc in the southern polarized ridge and up to 4 kpc in the western interarm space. If the radial extent of magnetic field is similar in those regions, this is likely to be the result of different diffusion coefficients for CRs propagating at various orientations to the mean magnetic field (see e.g. Giacalone & Jokopii 1999). The striking result is the lack of any ridge of total synchrotron radiation to the south of the SW arm, where the *polarized* synchrotron emission has a global maximum within the whole galaxy disk (Sect. 3.2). We explain this by 1) a relatively small contribution of polarized emission from ordered magnetic fields to the total synchrotron radiation here (polarization degree of about $p = 0.24\%$), and 2) gradual increase in actual synchrotron emission towards the galaxy's centre due to higher density of CRs and random magnetic fields.

4.3. Interrelations between gas phases

The interrelations between various ISM components in NGC 4254 were analysed using a spectral decomposition of the related images in the broad domain of spatial scales (Frick et al. 2001). Besides radio, X-ray, and optical data, we included the 24 μm mid-infrared (MIR) map from the Spitzer survey of SINGS galaxies (Kennicutt et al. 2003), revealing dust and PAH emission heated by young stars and IRAC 3.6 μm (near-infrared, NIR) map dominated by radiation from old stellar atmospheres. All maps were convolved to the same resolution of $15''$. The brightest point-like sources were subtracted from the maps. We applied the *Pet Hat* (PH) isotropic wavelet to derive the wavelet cross-correlation coefficient $r_{\rm w}$ at various spatial scales.

A high crosscorrelation ($r_{\rm w} \approx 0.8$) is observed between almost all species on the largest scales (Fig. 8), demonstrating the overall correspondence of their extended emission and hence the lack of spatial truncation in any gas phase. A lower correlation of hot ionized medium traced by our X-ray data with H I ($r_{\rm w} \approx 0.3$) reflects an extended envelope of neutral hydrogen discussed in Sect. 3.2.

The highest wavelet-correlations are visible between the various species of warm ionized medium (WIM) dominated by thermal processes. The highest correlation ($r_{\rm w} > 0.88$) is found between the radio thermal and mid-infrared emissions on all spatial

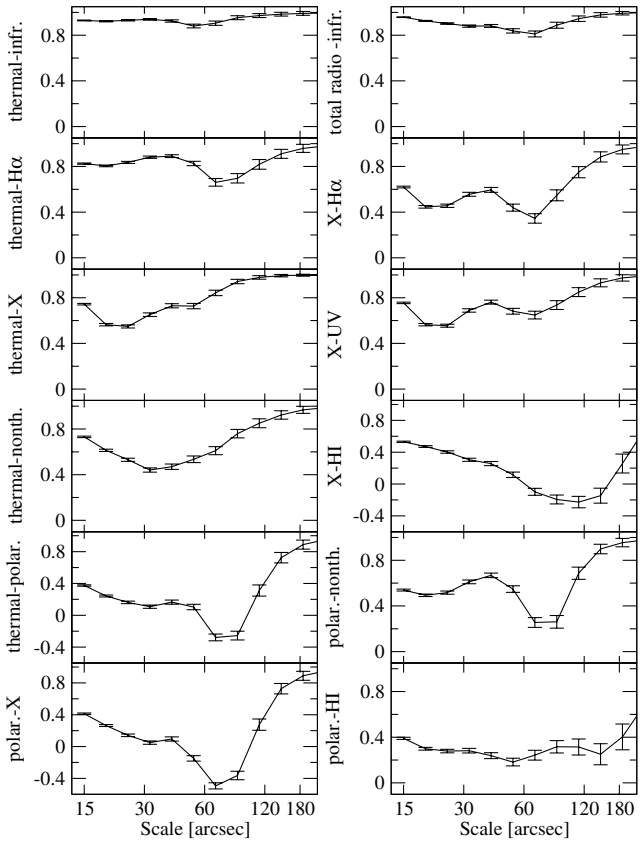

Fig. 8. Wavelet (PH) cross-correlation coefficients for some ISM species as a function of scale.

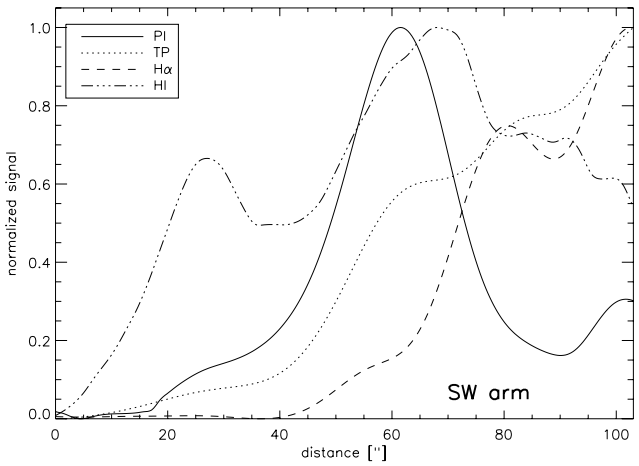

Fig. 9. The southern slice across the SW arm in polarized and total radio intensity at 4.86 GHz, as well as Hα and H I emission at 15″ resolution. The direction of the slice is from outside towards the disk centre (see Fig. 2, bottom-right panel, for the exact position). The location of the SW optical spiral arm is also marked.

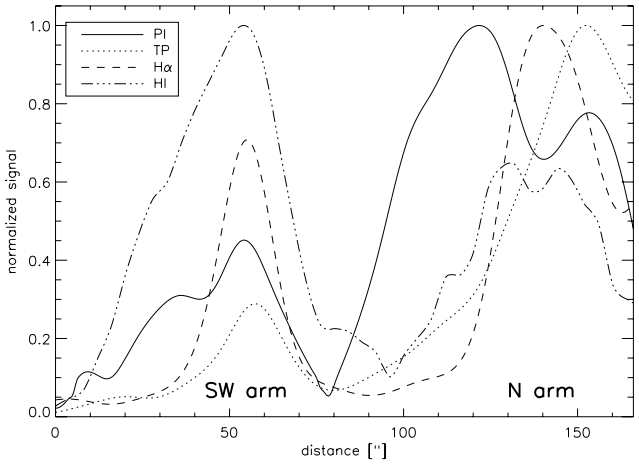

Fig. 10. The western slice across the interarm (N and SW) region. The details as in Fig. 9. The locations of optical spiral arms are marked.

scales, and between the total radio emission and the mid-infrared one ($r_w > 0.80$). Almost similarly high ($r_w \approx 0.80$) is the radio thermal-Hα correlation. The synchrotron emission is also connected to the thermal emission, although with weaker correlation ($r_w > 0.4$). Similar relations are observed in the grand-design spiral NGC 6946 (Frick et al. 2001), e.g. for the Hα-radio thermal emissions $r_w = 0.8$ and for the radio thermal-nonthermal one $r_w = 0.53$. This indicates that the cluster medium does not affect spatial interrelations between various ISM components in NGC 4254 and that they remain quite similar to those in the non-cluster and non-interacting spiral NGC 6946.

A completely different kind of relations is revealed by the polarized emission, which shows a decrease in correlation with other species on scales of about 1′ to 1.′5. In the case of thermal and X-ray emission it even amounts to anticorrelation, which was also observed in NGC 6946 ($r_w = -0.1$ for the radio polarized and thermal emission, Frick et al. 2001), but here is even stronger ($r_w = -0.4$). It is obviously caused by a distinct displacement of the southern polarized ridge from thermal (warm and hot) gas located in the NW spiral arm and by the other polarized features interlaced with optical arms (Sect. 3.2).

To investigate the phenomenon of polarized emission further in NGC 4254, we performed a slice across the southern polarized ridge in distributions of various ISM components. The slice (presented in Fig. 9) clearly shows a displacement of polarized intensity with respect to the optical arm by about 20″ (a maximum in the polarized intensity is located 60″ from the slice's beginning, while the Hα peaks at 80″). Moving towards the galaxy centre, both the optical and the total radio emission increase, while the polarized emission drops off steadily, possibly due to an enhanced star-forming activity, thus a larger ISM turbulence that disrupts the ordered field. There is a correspondence of the maximum in polarized emission with the enhancement of H I distribution, which also peaks outwards of the optical arm (at 70″). An additional rise in the H I distribution can be seen 40″ further out of the polarized ridge, but neither polarization nor other gas tracers are found here.

Can accumulations of H I gas alone driver the enhancements of polarized emission in NGC 4254? To test this idea we performed another slice through the western part of the galaxy across the N and SW arms (Fig. 10). The H I gas peaks now at the exact position of the optical SW arm (at 55″) and is associated with only a small peak in polarized emission (0.4 in normalized signal). However, the more than two times weaker H I emission around the N arm is accompanied by the global maximum in polarized intensity (1.0 in the normalized signal at 120″). This is quite contrary to the southern part of the disk, where polarized and H I maxima coincide.

It seems that the strongest polarized emission in NGC 4254 is enhanced more outside the optical arms by some external process independent of H I gas (see Sect. 4.6.3). Hence, the polarized emission behaves in a very different way than the other analysed ISM species and is significant in any modelling of

ISM evolution, providing us with independent information on the history of cosmic-ray and the magnetic-field evolution.

4.4. Radio thermal emission as a star-formation rate indicator

One of the best measures of evolutionary state of a galaxy and a sensitive indicator of some types of environmental interactions is SFR (e.g. Koopmann & Kenney 2004). Many SFR indicators based on luminosities from various spectral ranges have been used (e.g. Kennicutt 1998), but they all suffer from different flaws: the most common Hα-based SFR is severely contaminated by internal extinction, while the extinction-free, infrared-based SFR is affected by an unknown fraction of diffuse IR emission (cirrus component) and requires a high degree of dust opacity. Condon (1992) derived a commonly-used radio-nonthermal SFR indicator, based on empirical calibration of radio emission by the supernova rate within the Milky Way, which however may be not valid for all galaxies.

The most straightforward and accurate SFR indicator can be derived from the radio thermal emission, which is free of all these difficulties and, in addition, can be applied within a single galaxy. The most severe problem with this approach is the uncertainty of the thermal-nonthermal flux separation, which requires sensitive multi-frequency radio data. However, in the case of NGC 4254, the separation procedure proved to be reliable and allows us to estimate SFR in the individual regions of NGC 4254. For the first time, we confront the derived SFR *within* a spiral galaxy basing on thermal radio emission with the Hα-based SFR.

We used the map of radio thermal emission at 8.46 GHz and the map of Hα emission from Knapen et al. (2004) convolved to a common beam of 15″ HPBW. The Hα map was corrected for baselevel undulations using the task IMSURFIT in IRAF package. The background'd constant level was then subtracted and the image calibrated with the scaling factor of 38.0926 from Knapen et al. (2004). We corrected the Hα emission for foreground Milky Way extinction using $E(B-V) = 0.039$ (from LEDA). With the adopted distance of 16.8 Mpc to the galaxy, we derived a total Hα flux of 1.35×10^{-11} erg s^{-1}, which is in good agreement with Koopmann et al. (2001). Both maps were decomposed into beam-separated regions to determine values of radio thermal and Hα brightness. The radio thermal fluxes were then used to predict the extinction-free emission in the Hα line, H$\alpha_{\rm pred}$, according to the classical model of H II regions by Caplan & Deharveng (1986). Following this approach, we evaluated the predicted Hα emission from the thermal flux TH_ν at the frequency ν:

$$\left(\frac{\mathrm{H}\alpha_{\rm pred}}{\mathrm{erg\,s^{-1}\,cm^{-2}}}\right) = 3.5\times10^{-7}\,\frac{N(\mathrm{H^+})}{N(\mathrm{H^+})+N(\mathrm{He^+})} \times\left(\frac{T_\mathrm{e}}{\mathrm{K}}\right)^{-0.57}\left(\frac{\nu}{\mathrm{Hz}}\right)^{-0.1} TH_\nu. \quad (1)$$

For electron temperature we assumed a typical value of $T_\mathrm{e} = 10^4$ K, for abundance ratio $N(\mathrm{H^+})/N(\mathrm{He^+}) = 0.08$, and for frequency $\nu = 8.46$ GHz. The results depend weakly on the temperature and He/H ratio: raising the temperature to 1.2×10^4 K or the abundance ratio to 0.09 would change H$\alpha_{\rm pred}$ values by 10%. Both the observed Hα and predicted H$\alpha_{\rm pred}$ fluxes were converted to luminosities, adopting the distance of 16.8 Mpc to NGC 4254, and normalized to the area in kpc^2 in each independent region. These luminosities are plotted in Fig. 11, together with the corresponding SFRs derived from the extinction-free Hα calibrator (Kennicutt 1998).

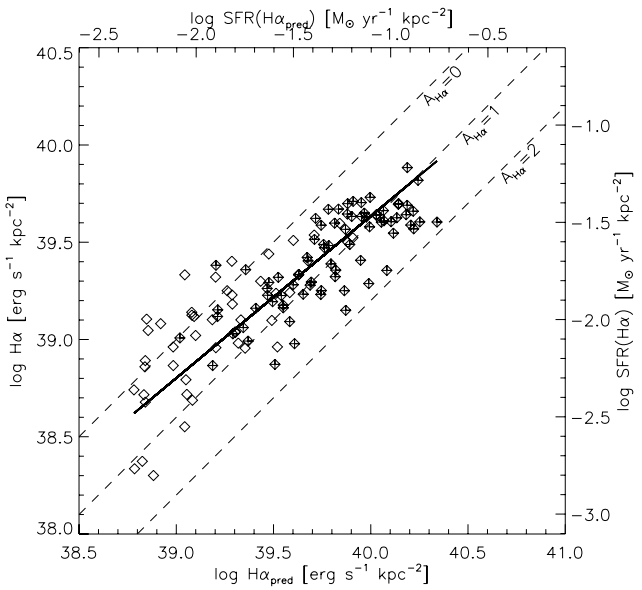

Fig. 11. The luminosities of Hα emission and the predicted extinction-free H$\alpha_{\rm pred}$ emission from the radio thermal data for the individual beam-separated regions of NGC 4254. The luminosities of all regions are normalized to the area in kpc^2. The crosses indicate the regions in the inner part of the galaxy with higher signal-to-noise ratio. The solid line shows the best-fit linear model, while the dashed lines represent internal Hα extinction values of 0, 1, and 2 mag. The corresponding SFRs are indicated on the top and right coordinate axes.

The predicted extinction-free Hα luminosities based on the radio thermal emission are on average higher than the measured Hα ones, as could be expected. The mean internal extinction for the whole galaxy is about 0.8 mag, but it seems to depend on luminosity: for low luminosities of about 10^{39} erg s^{-1} kpc^{-2}, it is about 0.5 mag and systematically rises to about 1.0 mag at 2×10^{40} erg s^{-1} kpc^{-2}. This behaviour is quantified by a linear fit to the data, using the bisector method by Isobe et al. (1990), giving

$$\log(\mathrm{H}\alpha) = (6.3 \pm 2.2) + (0.83 \pm 0.06)\log(\mathrm{H}\alpha_{\rm pred}) \quad (2)$$

or in other form:

$$A_{\mathrm{H}\alpha} = (0.42 \pm 0.15)\log(\mathrm{H}\alpha_{\rm pred}) - (18.8 \pm 5.5). \quad (3)$$

The observed rise in extinction with Hα emission can be explained by a larger amount of dust and CO gas within intense star-forming regions. To check for possible influencing this relation by regions with lower signal-to-noise ratio, typically found in the outer parts of the galaxy, (Fig. 11), we performed a similar fit without them. The results are very similar and the slope in the first relation above is 0.80 (±0.05) in this case.

According to our findings, the mean SFR of NGC 4254 as a whole is 0.026 $M_\odot$ yr^{-1} kpc^{-2}, about 3 times larger than in the nearby normal galaxies of similar Hubble types (see Kennicutt 1998). This result is contrary to the main trend among Virgo Cluster spirals, which show SFR reduced by a factor up to 2.5 as compared to isolated objects (Koopmann & Kenney 2004). The reduction in the SFR was found in galaxies with spatially truncated Hα distribution in the outer disk portions and is explained by a stripping process exerted by the ram pressure of hot ICM (see also Sect. 4.6.1).

Finally, as a check for consistency, we compare the *global* SFR derived for NGC 4254 in Table 3 using various indicators

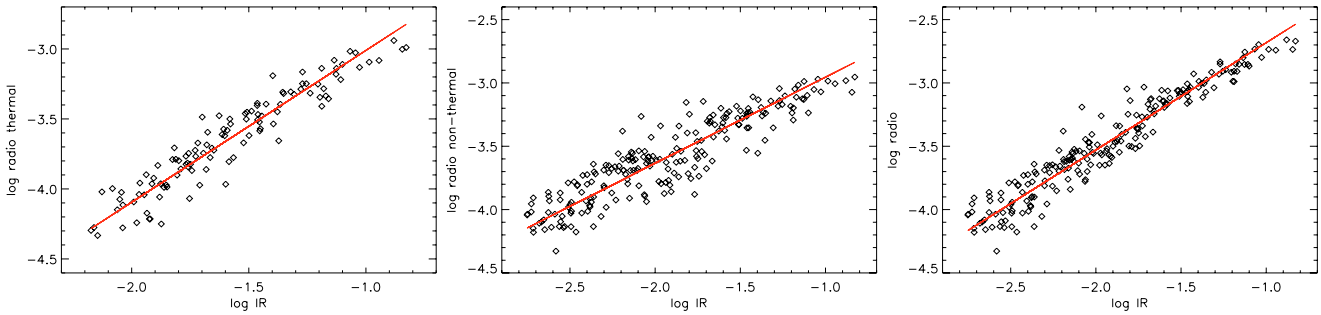

Fig. 12. Radio-infrared correlations for radio thermal (*left*), nonthermal (*middle*) and total (*right*) emission at 8.46 GHz at 15″ resolution within beam-separated regions of NGC 4254.

Table 3. Global SFRs for NGC 4254, corrected (where necessary) for Milky Way extinction.

Method	SFR $[M_\odot\ \mathrm{yr}^{-1}]$
Thermal radio $L_{\mathrm{H}\alpha\mathrm{pred}} = 1.1 \times 10^{42}$ erg s^{-1}	8.4
Total radio $L_{1.4} = 1.62 \times 10^{29}$ erg s^{-1} Hz^{-1}	9.6
MIR $L_{24\ \mu\mathrm{m}} = 1.39 \times 10^{30}$ erg s^{-1} Hz^{-1}	7.1
Hα $L_{\mathrm{H}\alpha} = 5.0 \times 10^{41}$ erg s^{-1}	4.0

according to Kennicutt (1998). We assume the Salpeter IMF in the range of 0.1−100 $M_\odot$ in each case. The infrared estimation (7.1 $M_\odot$ yr^{-1}) and our radio thermal emission indicator (8.4 $M_\odot$ yr^{-1}) agree within the errors of calibration, which are about 10% and 5% in the MIR and radio bands, respectively. The SFR value derived from the total radio luminosity at 1.43 GHz exceeds the one based on the infrared emission by 35%. The difference is physically relevant. At this frequency the total radio flux is largely dominated by synchrotron emission, which is nonlinearly related to SFR with an exponent larger than 1 (Niklas & Beck 1997, see also next section). This makes the nonthermal radio indicator less precise and subject to systematic bias. The Hα-based SFR is underestimated (by a factor of about 2), and if not corrected for dust extinction can lead to serious errors.

4.5. Radio thermal – nonthermal – IR relations

The well-known global correlation of the radio and infrared emission of galaxies (Helou et al. 1985) was demonstrated to be present in our vicinity, as well as in the distant Universe (Appleton et al. 2004). The underlying physical processes of this relation obviously act on much smaller scales than galaxy sizes, but our understanding of them is still incomplete. Taking the opportunity of Spitzer's recent high-resolution observation of warm dust of NGC 4254 at mid-infrared 24 μm, we investigated the radio-infrared relation *within* this galaxy separately for the thermal and nonthermal radio components decomposed in Sect. 4.2. Performing such a study for the first time for a cluster galaxy is of special interest, as the influence of the cluster environment on the radio-IR relation is still unknown and NGC 4254 distinctly shows a disturbed morphology in all spectral bands, as well as enhanced processes of star formation (Sect. 4.4).

The infrared emission and the components of radio intensity at 8.46 GHz are derived in the beam-separated regions within NGC 4254 at a resolution of 15″ (Fig. 12). The relations are quantified by bisector linear fitting to the logarithms of intensities of different radio components (Y) and IR 24 μm fluxes (X). The resulting slopes are given in Table 4, together with

Table 4. The radio-infrared correlation within NGC 4254.

Y – X	slope α	r	N
Radio-thermal – IR	1.08 ± 0.03	0.95	113
Radio-nonthermal – IR	0.68 ± 0.02	0.90	210
Radio-total – IR	0.85 ± 0.02	0.96	210

the Pearson correlation coefficients r, and number of beam-separated regions N used.

The relationship for NGC 4254 between radio thermal and infrared radiation (the slope $\alpha = 1.08 \pm 0.03$) differs considerably from the relation with the nonthermal component ($\alpha = 0.68 \pm 0.02$). The slope of the total radio/infrared correlation lies in between the two above ($\alpha = 0.85 \pm 0.02$), closer to the dominant nonthermal component. All the relations are statistically highly significant (with correlation coefficients $r \geq 0.90$). The relation with the total radio emission is the closest one (Fig. 12). It is measured in a quantitative manner by the residual dispersion of the fit. In the case of thermal and nonthermal emission, these dispersions are 0.16 and 0.14, respectively, and just 0.10 for the total emission.

Comparing the obtained slope for the local nonthermal-IR correlation in NGC 4254 with the other galaxies studied to date (which include non-cluster galaxies: M 31, Hoernes et al. 1998; M 83, Vogler et al. 2005; NGC 6946, Walsh et al. 2002; and the Large Magellanic Cloud, Hughes et al. 2006), we notice that the slope is always less than one ($\alpha < 1$). Hence, this seems to be a general phenomenon that does not depend on the galactical morphology, Hubble type, and cluster membership. However, the slope is >1 for the *global* correlation (Niklas & Beck 1997). We propose that the differences are probably due to propagation effects: the UV photons heating the dust can partly escape from the star-forming regions, while the CR electrons produced in those regions also escape but on different temporal and spatial scales. Therefore the nonthermal emission in star-forming regions is reduced, but the infrared radiation remains strong. This is well described well by a phenomenological model in which a radio image appears as a "smeared" version of the IR image (Murphy et al. 2006).

Another explanation for the flat local nonthermal-infrared correlation is the method of thermal-nonthermal separation. In star-forming regions the nonthermal spectral index could be flatter than 1.0 due to the direct contribution from young supernova remnants (index ≈0.5). This means that the thermal emission might be overestimated, meaning the nonthermal emission can be underestimated in these regions, too. However, this cannot explain why the slope of the local correlation between the *total* radio and IR emission is also flatter than 1.

The comparison of radio thermal-IR relation for NGC 4254 with the other galaxies reveals another trend for the slope of this relation to rise systematically with IR-wavelengths: from 0.8 and 0.9 for 7 μm and 15 μm, respectively, for NGC 6946 (Walsh et al. 2002); through our 1.08 for 24 μm for NGC 4254; up to 1.17 and 1.31 for 60 μm and 100 μm for M 31 (Hoernes et al. 1998). NGC 4254 follows this trend, again showing that its interaction with the cluster environment does not affect the slope of the correlation. At the same time, the correlation coefficient reaches its maximum at 24 μm for NGC 4254 ($r = 0.95$), which we recognise as the wavelength at which the thermal processes that power radio emission and heat the dust are coupled best. In a recent study, Tabatabaei et al. (2007a) points out that, besides the dust heating by ionizing UV flux from massive stars, an aditional dust heating from intermediate-mass and solar-mass stars may contribute to the emission of the colder dust component seen at longer IR wavelengths.

The observed differences between the correlation slopes of thermal and nonthermal emission versus the infrared radiation in NGC 4254 can lead to a steeper *total* radio-IR relation for the regions with a higher thermal fraction. Such a tendency could explain the recent findings of Hughes et al. (2006), who analysed the total radio (1.4 GHz)-IR relation within regions of various star-forming intensity of the Large Magellanic Cloud.

We also compared the *global* radio-infrared properties of NGC 4254 with the other nearby field galaxies using the surface brightness at 4.86 GHz and 60 μm: NGC 4254 fits very well with the general trend of a close radio-IR correlation (see Chyży et al. 2006). Among 19 galaxies of Sc type, NGC 4254 has the second highest surface brightness both in the infrared and radio domains. Thus, the observed strong radio emission cannot be attributed to the total magnetic field locally compressed by e.g. ram pressure of hot ICM. Such a mechanism has been suggested to explain the high radio luminosity of Coma cluster galaxies (Gavazzi et al. 1991). We propose that the agent to enhance the SFR in NGC 4254 (most likely the gravitational interaction, Sect. 4.4) also increases (by thermal and nonthermal processes) the infrared and radio emission. This explains the strong radio-MIR wavelet correlation observed in NGC 4254 on all spatial scales (Sect. 4.3), as well as why the close radio-IR relations revealed by non-cluster spirals are also valid for this galaxy. Although the external interactions do not seem to influence the global radio-IR relation for galaxies like NGC 4254, they do affect the polarized radio intensity. As a result, the polarization observations are apparently the key to revealing a perturbing agent that is not seen, or barely seen, in other ISM components.

4.6. Scenarios of interaction

4.6.1. Ram pressure

From the available H I velocity field alone (Fig. 13), we cannot decide whether NGC 4254 moves inwards or outwards from the Virgo cluster centre. If the galaxy is just entering the Virgo cluster, it can currently experience ram pressure on the southern disk side by hot ICM. This was an early idea by Cayatte et al. (1994) to explain the global N–S asymmetry in the distribution of the H I gas (see also Sect. 3.1). In this scenario, the southern radio-polarized ridge could be explained by compression of magnetic field at the ISM/ICM interface. Such ram-pressure effects should also spatially truncate the Hα distribution at the outer disk portion, as shown for a number of other Virgo cluster spirals (Koopmann & Kenney 2004). To check this hypothesis, we compared Hα with the NIR emission (3.6 μm) representing

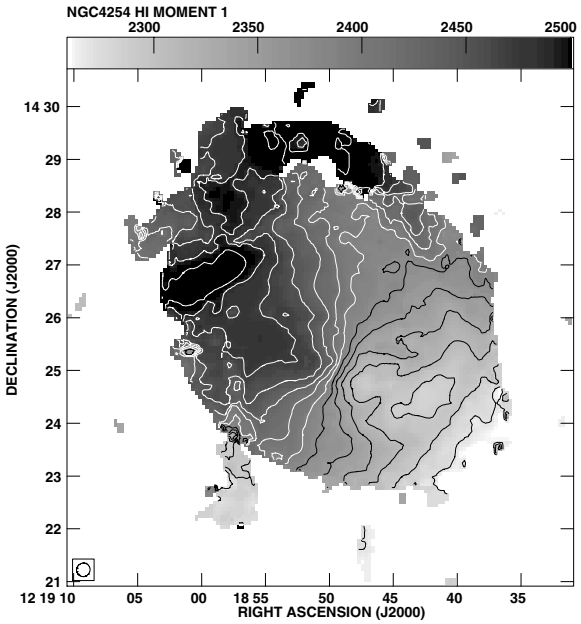

Fig. 13. The VLA (archive re-reduced) H I isovelocity contours of NGC 4254 (in km s^{-1}) and the greyscale of H I velocity field. The beam size is 15″ HPBW. The isovelocity contours correspond to 2.27, 2.29, 2.31, 2.33, 2.35, 2.37, 2.39, 2.41, 2.43, 2.45, 2.47, 2.49, 2.51 × 10^3 km s^{-1} starting from from SW towards NE.

the old stellar population in NGC 4254, which should not be affected by ram pressure (Fig. 1). Both the distributions reveal a complex/disturbed spiral pattern, while there is no evidence of either any reduction of Hα emission in the southern outer disk or any systematic displacement from the NIR radiation. A similar plot made for e.g. the Virgo Cluster spiral NGC 4522, believed to be ram pressure stripped, clearly demonstrates a truncated Hα disk, as well as extraplanar gas (Kenney & Koopmann 1999).

In agreement with that, NGC 4254 does not reveal any truncation in synchrotron emission or in total radio emission, even at the longest wavelength analysed (Sect. 3.1). Our wavelet cross-correlation analysis (Sect. 4.3) also indicates similar distributions of various ISM gas phases on the largest spatial scales and the presence of an extended H I envelope. The global distortion of the galactic spiral pattern observed in all analysed spectral bands cannot be an argument for ram pressure effects as they do not affect stars.

To test the importance of ram pressure versus other competing forces locally in the southern disk of NGC 4254, we compared their corresponding energy densities. We chose a small region of 15″ in the southern polarized ridge, marked in Fig. 2 (bottom-right panel). For calculating the ram pressure ρV^2, we assumed a galaxy velocity $V = 1000$ km s^{-1} from the hydrodynamical modelling of Vollmer et al. (2005). The density ρ of the hot cluster's gas was estimated from the profiles of Schindler et al. (1998), which for the location of NGC 4254 give $\rho = 6.2 \times 10^{-5}$ cm^{-3}. To calculate the energy density of turbulent gas motions, we assumed a typical turbulent velocity of cold gas of about 10 km s^{-1}. We took the H I gas density in the ridge and the CO gas density in its eastern part (at the edge of the available CO map from Sofue et al. 2003), as well as 0.2 kpc disk thickness, which gives an estimate of total gas density in the ridge as 3.2 cm^{-3}. Finally, from the radio thermal emission we estimated the thermal energy of WIM assuming a typical filling factor of

Table 5. The energy density of different species in the polarized ridge of NGC 4254 in comparison with the ram pressure of ICM and the kinetic energy of the infalling H I clouds.

Method	Energy density 10^{-12} erg cm^{-3}
Ram pressure of ICM	0.5
Kinetic energy of H I plume	1.6–3.2[a]
Turbul. energy (CO+HI)	5.3
Thermal energy of WIM	0.8–1.1[b]

[a] For various assumptions concerning geometry of the plume.
[b] For assumed different thermal disk thickness (0.2 and 0.1 kpc).

gas of about 0.05 and a thermal disk thickness of 0.1 kpc and 0.2 kpc.

The comparison of energy densities presented in Table 5 shows that the cluster ram pressure and the thermal energy of WIM are considerably (at least five times) lower than the energy in turbulent gas motions. Thus we find no evidence for ram pressure operating currently in NGC 4254.

If the galaxy is now receding from the cluster core it could pass through it earlier, experiencing strong ram pressure by the hot and dense ICM in the past. If the observed extraplanar H I clouds (Sect. 3.1) did result from such a past event, we should expect a deficiency in H I gas due to ISM-ICM stripping. However, this is not the case (Cayatte et al. 1994). Besides, given the galaxy's current large distance from M 87 (≈1 Mpc) and typical dispersion speeds of cluster members (see Vollmer et al. 2005), we estimate that this passage could have happened about 1.2 Gyr ago, which is more than two galactic revolutions. Such a time is long enough for winding up all the stripped material and for the turbulent decay of enhanced magnetic field, a time scale of about 3×10^8 yr (Widrow 2002).

4.6.2. Tidal interaction

If the distortion of spiral structure in NGC 4254 with its heavy SW arm does not have a ram pressure origin, it must have been caused by gravitational (tidal) interaction. No other process is able to influence the stellar orbits to the observed extent. There are two possible candidates for such an interaction. The first one is the recently discovered dark galaxy VIRGOHI 21 (Minchin et al. 2005), located to the north of NGC 4254 at a distance of about 150 kpc in the direction of the chain of observed weak H I plumes (see also Fig. 14 in the Online Material). However, its large mass (10^{11} $M_\odot$) speculated from its rotation curve has yet to be confirmed. The second candidate is the spiral galaxy NGC 4262 with a well-established large mass. It is also located north of NGC 4254, but it is not disturbed and the chain of H I blobs do not seem to be related to it (Minchin et al. 2005). According to numerical simulations (Vollmer et al. 2005), NGC 4254 might have suffered from a gravitational encounter some 10^8 yr ago.

Another argument for gravitational interactions is provided by our SFR analysis (Sect. 4.4). The galaxy's mean SFR is enhanced but not spatially truncated. This kind of external influence on the Virgo cluster spirals is indeed well-recognised as resulting from tidal interactions (Koopman & Kenney 2004). An SFR enhancement was also observed in the gravitationally interacting Antennae galaxies (Chyży & Beck 2004). The steep global radio-spectral index in NGC 4254 of 0.8 (Sect. 4.1) indicates an evolved population of star-forming regions, in agreement with a star formation triggered by gravitational encounter occurring a considerable time ago.

The global N–S asymmetry in the H I gas seen in the low-resolution (40″) data by Cayatte et al. (1994) appears at a higher resolution of 15″ to be composed of disk and out-of-disk components (Fig. 13). The external gas can be discerned well in the NE as a huge H I arc with a different velocity from the gas in the disk (also recognised by Phookun et al. 1993). Our second moment map of the H I velocity field (Fig. 15, available in the Online Material) does show an enhanced velocity dispersion to above 20 km s^{-1} at the point where the arc enters the disk from the north (RA = $12^h18^m44^s$, Dec = 14°28′0″). This region is rather small (40″ × 40″) and resembles the place in the southern disk where a single elongated H I blob starts to penetrate the disk. This favours the idea of the arc as a debris feature of a past gravitational encounter. In the case of gas pushed out from the disk by ram pressure, we should not expect a sudden, but a gentle and wide, distortion of the velocity pattern, as can be seen e.g. in the H I tail of NGC 4654 (Phookun & Mundy 1995).

Support comes from the inspection of recent Fabry-Perot observations in the Hα line (Chemin et al. 2006) showing a very regular disk rotation without any counterpart of the H I arc. Similarly, we did not find any associated magnetized plasma traced by the extended radio envelope at 1.43 GHz (Sect. 3.1) or any other ISM component. Thus, the H I arc and the global N–S asymmetry of H I gas is explained better by gravitational interaction than by the ram pressure hypothesis.

4.6.3. The puzzle of the polarized emission

NGC 4254 seems to belong to the class of "young" Virgo cluster members that recently experienced a gravitational encounter at the cluster's periphery. This perturbed its spiral arms by tidal forces and triggered a burst of star-formation that is still at a high level (Sect. 4.4) and maintains strong radio and infrared emissions (Sect. 4.5). The southern polarized ridge is, however, much more difficult to account for because it has no visible counterpart in the other spectral ranges (Sect. 3.2), and partly because such a strong magnetic structure lying *downstream* of the spiral density wave has been never observed in any other galaxy.

Within the framework of gravitational interaction, the enhanced polarized emission in the southern disk could potentially be caused by compressing plasma and the magnetic field by the tidally stripped H I gas falling now back onto the disk. To check this possibility, we calculated the ram pressure exerted by the large southern blob visible in Fig. 14. This blob is probably entering the disk with a relative velocity of about 100 km s^{-1} (Fig. 13). The mean gas density in the blob is 0.08 cm^{-3} and 0.04 cm^{-3} for the gas thickness values of 1 kpc and 2 kpc, respectively. According to our estimates (Table 5), the energy associated with returning cold gas is comparable to the thermal energy, but two times lower than the turbulent energy in the disk. The blob does not seem to affect either the strength or the orientation of magnetic field in the disk (Fig. 2), which may indicate that it moves along the orbit inclined to the disk. Both these arguments seem to exclude the hypothesis of plasma compression by returning cold gas, but the definite answer could bring only a careful MHD modelling of this interaction.

We also consider another possibility that the same tidal forces that disturbed the galactic stellar and gaseous content could also stretch and shear magnetized plasma along the SW spiral arm. This should result in transforming the random (isotropic) magnetic field component to an anisotropic one and locally enhancing the polarized radio emission

(cf. Sokoloff et al. 1998). As this emission constitutes just about 24% of the total one, it is obvious why such effects cannot be found in total radio emission and other ISM components. Whether the ridge can be actually caused by shearing cannot be established without quantitative modelling the magnetic field components. This will be attempted in Paper II.

We still cannot exclude the possibility that some *weak* ram pressure effects from hot ICM gas are still sufficient for modifying/compressing the magnetic field in the southern ridge, while not affecting other ISM components. This would mean that magnetic fields in NGC 4254 are much more sensitive to compressional forces than all other ISM phases. This hypothesis can be tested by a thorough MHD modelling of plasma, which is quite challenging as it requires accurate reconstruction of the gravitational encounter, the pattern of spiral density waves, and their influence on the different components of magnetic field.

In contrast to the radio thermal component, which correlates highly with the other species of thermal origin (Sect. 4.3), the radio polarized signal in NGC 4254 is not closely connected with the other ISM agents and in fact even anticorrelates with most of them in the southern polarized ridge. Follow-up studies of other galaxies in the Virgo cluster are needed to fully understand the role of magnetic field and environmental effects in cluster galaxies. The case of NGC 4254 shows that the polarized signal provides additional information on MHD processes acting on magnetized plasma during the galaxy's evolution, which cannot be obtained from any other ISM component. The analysis presented also shows that only high-resolution (1 kpc-scale) and multifrequency studies are appropriate for discerning various environmental processes influencing galaxies within clusters.

5. Summary

We present the first comprehensive investigation of the weakly perturbed Virgo cluster spiral NGC 4254. We performed VLA radio polarimetric observations at 8.46 GHz, 4.86 GHz, and 1.43 GHz, with sensitivity to extended structures enhanced by single-dish 100-m Effelsberg observations at the former two frequencies. We also carried out observations of hot gas components in X-ray and UV emission with the XMM-Newton satellite and re-analyzed H I observations obtained by Phookun et al. (1993). On the basis of our data and images in other spectral domains, we investigated the interrelations between different gas phases, as well as the influence of the cluster environment on the galaxy's morphology, especially in the radio domain.

We found the following:

1. The distributions of total radio intensity at 4.86 GHz and 8.46 GHz are disturbed. In the north, the emission is more diffuse and extends two times further than in the south. It follows the galaxy's optical images, thus the stellar and gaseous content of the unusual three-arm spiral structure. The strongest emission comes from the central disk region, where a bar-like structure can be discerned at the highest (7.″5) radio resolution available, corresponding to a similar feature appearing in CO emission (Sofue et al. 2003).
2. The polarized part of synchrotron emission at 8.46 GHz and 4.86 GHz is highly asymmetric and shows a strange, sharp, and bright, ridge in the southern disk *shifted outwards* of the optical SW spiral arm, downstream of the density wave. There is a high degree of polarization in this region, locally reaching 40% (and a mean value of 24%). Three other polarized ridges are interlaced with adjacent optical spiral arms, while still another one is aligned with them. This complex mixture of magnetic field patterns, as well as the strong global asymmetry of polarized emission, is very unusual among spiral galaxies observed so far at such high radio frequencies.
3. The orientations of magnetic field vectors vary strongly over the galaxy, from almost zero apparent magnetic pitch angles in the south up to 30°–40° in the northern part, but they are mainly aligned (within 20°) with orientations of optical arms. We report the discovery of a large magnetized radio envelope of NGC 4254 at 1.43 GHz with ordered magnetic fields extending further outwards (4 kpc) than the warm and hot gas.
4. Our XMM-Newton data reveal some soft X-ray emission tightly associated with star-forming regions almost from the whole galactic disk. The X-ray distribution is disturbed along a similar pattern to radio and optical emission and shows no out-of-disk emission or shocks that could imply strong ram pressure forces.
5. The wavelet decomposition of images reveals the highest wavelet crosscorrelation between various species dominated by thermal processes, especially between radio thermal and 24 μm mid-infrared emission (correlation coefficients $r_\mathrm{w} \geq 0.88$ at all inspected spatial scales). However, the polarized emission anticorrelates ($r_\mathrm{w} = -0.4$) with the radio thermal and X-ray emission, manifesting the displacement of magnetic arms from the optical ones. These results are quite similar to the non-cluster spiral NGC 6946 (Frick et al. 2001).
6. For the first time, we have used the radio thermal emission at 8.46 GHz to derive an extinction-free SFR distribution across the galaxy. We find higher extinction values in more Hα luminous star-forming regions with a power-law slope of 0.83. The estimated mean SFR over the galactic disk of 0.026 $M_\odot$ yr^{-1} kpc^{-2} (corresponding to a global SFR of 8.4 $M_\odot$ yr^{-1}) is higher than in typical field spirals of the same Hubble (Sc) type. Contrary to the main trend among Virgo Cluster spirals, the star-forming disk in NGC 4254 is neither spatially truncated nor shifted from the old stellar population, which excludes strong ram-pressure stripping by hot ICM.
7. Investigating the *local* radio-IR relation for the first time for a disturbed cluster spiral, we found for NGC 4254 a strong correlation ($r \geq 0.90$) of radio thermal, nonthermal, and total emission at 8.46 GHz with 24 μm (MIR) radiation. The obtained flat slope (<1) for the local *nonthermal*-IR relation differs from the *thermal*-IR one (≥1). We argue that the thermal process that powers the radio emission is best coupled with dust heating at 24 μm. We find that NGC 4254 is consistent with the *global* radio-IR relationship determined for the field galaxies.
8. The idea of the ram pressure of hot ICM acting on the galaxy disk is questionable in view of the analysed multifrequency data. We argue that the spiral arm pattern has been perturbed by tidal forces, which both induced a strong star-formation rate and sheared the magnetic field in the southern disk along the optically bright SW spiral arm, leading to the strong polarized ridge. In order to make sure this process could be common among other disturbed spirals in the Virgo Cluster, similar comprehensive and multifrequency studies of them are desirable.

Acknowledgements. The Authors wish to express their thanks to Dr Igor Patrikeev for help in the wavelet calculations and to Dr J. Knapen for assistance in calibrating the Hα image. We are also grateful to Prof. M. Urbanik, Dr M. Krause, and the anonymous referee for valuable comments. This work

was supported by a grant from the Polish Research Committee (KBN), grant No. PB249/P03/2001/21.

References

Appleton, P. N., Fadda, D., Marleau, F. R., et al. 2004, ApJ, 154, 147
Beck, R. 2000, in The Interstellar Medium in M 31 and M 33, ed. E. M. Berkhuijsen et al., Proceedings 232nd WE-Heraeus Seminar (Aachen: Shaker), 171
Beck, R. 2004, in How does the galaxy work?, ed. W. J. Alfaro et al. (Dordrecht: Kluwer), 277
Beck, R. 2005, in Cosmic Magnetic Fields, ed. R. Wielebinski, & R. Beck (Heidelberg: Springer), 41
Beck, R. 2007, A&A, 470, 539
Beck, R., & Hoernes, P. 1996, Nature, 379, 47
Binggeli, B., Popescu, C. C., & Tammann, G. A. 1993, A&AS, 98, 275
Böhringer, H., Briel, U. G., Schwarz, R. A., et al. 1994, Nature, 368, 828
Boselli, A., & Gavazzi, G. 2006, PASP, 118, 517
Briggs, D. 1995, Ph.D. Thesis, New Mexico Inst. Mining Tech.
Caplan, J., & Deharveng, L. 1986, A&A, 155, 297
Cayatte, V., Kotanyi, C., & Balkovski, C. 1994, AJ, 107, 1003
Chemin, L., Balkowski, C., Cayatte, V., et al. 2006, MNRAS, 366, 812
Chyży, K. T. 2007, A&A, Paper II, in prep
Chyży, K. T., & Beck, R. 2004, A&A, 417, 541
Chyży, K. T., Soida, M., Bomans, D. J., et al. 2006, A&A, 447, 465
Condon, J. J. 1992, ARA&A, 30, 575
Dale, D. A., Helou, G., Contursi, A., Sibermann, N. A., & Kolhatkar, S. 2001, ApJ, 549, 215
Ehle, M., & Beck, R. 1993, A&A, 273, 45
Frick, P., Beck, R., Berkhuijsen, E. M., & Patrickeyev, I. 2001, MNRAS, 327, 1145
Gavazzi, G., Boselli, A., & Kennicutt, R. 1991, AJ, 101, 1207
Giacalone, J., & Jokipii, J. R. 1999, ApJ, 520, 204
Gonzáles, R. A., & Graham, J. R. 1996, ApJ, 460, 651
Helou, G., Soifer, B. T., & Rowan-Robinson, M. 1985, ApJ, 298, L7
Hoernes, P., Berkhuijsen, E. M., & Xu, C. 1998, A&A, 334, 57
Hughes, A., Wong, T., Ekers, R., et al. 2006, MNRAS, 613, 1
Hummel, E., & Beck, R. 1995, A&A, 303, 691
Isobe, T., Akritas, E. I., & Babu, G. J. 1990, ApJ, 365, 104
Jansen, F., Lumb, D., Altieri, B., et al. 2001, A&A, 365, L1
Kenney, J. D. P., & Koopmann, T. A. 1999, AJ, 117, 181
Kenney, J. D. P., van Gorkom, J. H., & Vollmer, B. 2004, AJ, 127, 3361
Kennicutt, R. C. 1998, ARA&A, 36, 189
Kennicutt, R. C., Armus, L., Bendo, G., et al. 2003, PASP, 115, 928
Knapen, J. H., de Jong, R. S., Stedman, S., & Bramich, D. M. 2003, MNRAS, 344, 527
Knapen, J. H., Stedman, S., Bramich, D. M., Folkes, S. F., & Bradley, T. R. 2004, A&A, 426, 1135
Koopmann, R. A., & Kenney, J. D. P. 2004, ApJ, 613, 851
Koopmann, R. A., Kenney, J. D. P., & Young, J. 2001, ApJS, 135, 125
Krause, M. 1993, in The Cosmic Dynamo, ed. F. Krause, K.-H. Räler, & G. Rüdiger (Dordrecht: Kluwer), IAU Symp., 157, 305
Krause, M., Hummel, E., & Beck, R. 1989, A&A, 217,4
Machacek, W. E., Jones, C., & Forman, W. R. 2004, ApJ, 610, 183
Mason, K. O., Breeveld, A., Much, R. et al. 2001, A&A, 365, L36
Minchin, R. F., Davies, J. I., Disney, M. J., et al. 2005, ApJ, 622, L21
Morsi, H. W., & Reich, W. 1986, A&A, 163, 313
Murphy, E. J., Helou, G., Braun, R., et al. 2006, ApJ, 651, L111
Neininger, N., Beck, R., Sukumar, S., & Allen, R. J. 1993, A&A, 274, 687
Niklas, S. 1995, Thesis, Univ. Bonn
Niklas, S., & Beck, R. 1997, A&A, 320, 54
Niklas, S., Klein, U., & Wielebinski, R. 1997, A&A, 322, 19
Patrikeev, I., Fletcher, A., Stepanov, R., et al. 2006, A&A, 458, 441
Phookun, B., & Mundy, L. G. 1995, ApJ, 453, 154
Phookun, B., Vogel, S. N., & Mundy, L. G. 1993, ApJ, 418, 113
Rasmussen, J., Ponman, T. J., & Mulchaey, J. S. 2006, MNRAS, 370, 453
Schindler, S., Bingelli, B., & Böhringer, H. 1999, A&A, 343, 420
Sofue, Y., Koda, J., Nakanishi, H., & Hidaka, M. 2003, PASJ, 55, 75
Soida, M., Urbanik, M., & Beck, R. 1996, A&A, 312, 409
Soida, M., Urbanik, M., Beck, R., Wielebinski, R., & Balkowski, C. 2001, A&A, 378, 40
Sokoloff, D. D., Bykov, A. A., Shukurov, A., et al. 1998, MNRAS, 299, 189
Strüder, L., Briel, U., Dennerl, K., et al. 2001, A&A, 365, L18
Tabatabaei, F., Beck, R., Krause, M., et al. 2007a, A&A, 466, 509
Tabatabaei, F., Krause, M., & Beck, R. 2007b, A&A, submitted
Turner, M. J. L., Abbey, A., Arnaud, M., et al. 2001, A&A, 365, L27
Vallée, J. P. 2004, New Astron. Rev., 48, 763
Vogler, A., Madden, S. C., Beck, R., et al. 2005, A&A, 441, 491
Vollmer, B., Cayatte, V., Balkowski, C., & Dushl, W. J. 2001, ApJ, 561, 708
Vollmer, B., Huchtmeier, W., & van Driel, W. 2005, A&A, 439, 921
Walsh, W., Beck, R., Thuma, G., et al. 2002, A&A, 388, 7
Widrow, L. M. 2002, Rev. Mod. Phys., 74, 775

Online Material

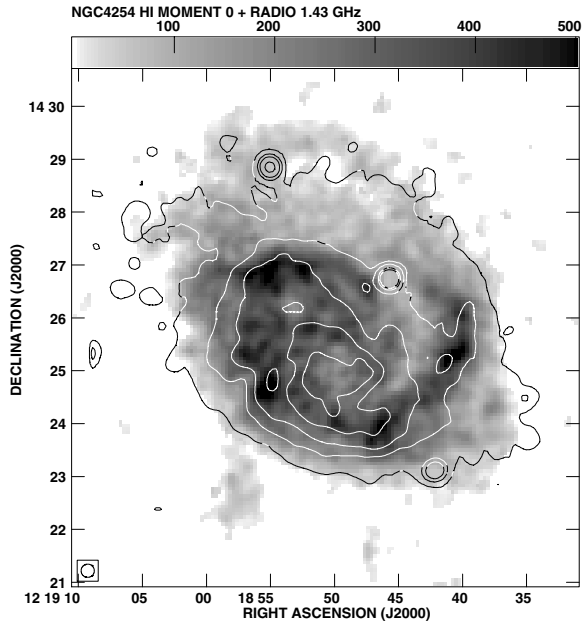

Fig. 14. VLA (archive re-reduced) H I intensity of NGC 4254 in greyscale (in Jy b.a.$^{-1}$ km s^{-1}) and the radio continuum emission at 1.43 GHz in contours. The beam size is 15″ HPBW.

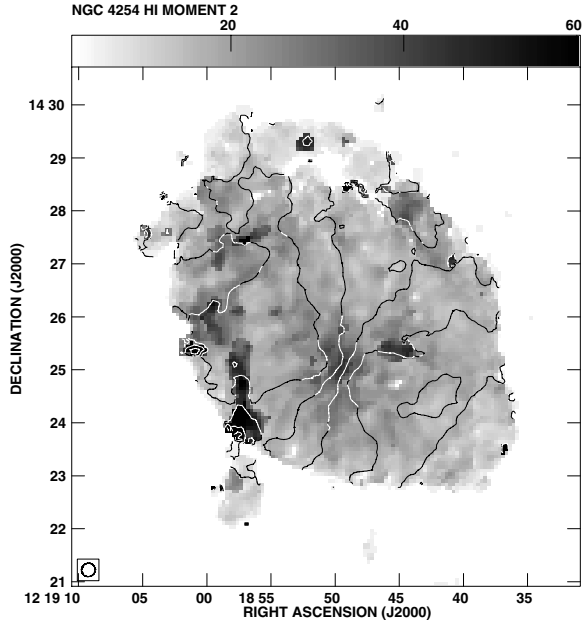

Fig. 15. Velocity dispersion of H I gas in NGC 4254 (in km s^{-1}) in greyscale with isovelocity contours at 2.29, 2.33, 2.37, 2.41 × 10^3 km s^{-1} (see also Fig. 13). The VLA (archive re-reduced) data have the beam size of 15″ HPBW.